

## Extreme smog challenge of India intensified by increasing lower tropospheric stability

Ritesh Gautam<sup>1\*†</sup>, Piyushkumar N. Patel<sup>2,3†</sup>, Manoj K. Singh<sup>4</sup>, Tianjia Liu<sup>5</sup>, Loretta J. Mickley<sup>6</sup>, Hiren Jethva<sup>3,7</sup>, Ruth S. DeFries<sup>8</sup>

<sup>1</sup>Environmental Defense Fund, Washington DC, USA.

<sup>2</sup>NASA Jet Propulsion Laboratory, Pasadena, CA, USA.

<sup>3</sup>Universities Space Research Association, Columbia, MD, USA.

<sup>4</sup>School of Engineering, University of Petroleum and Energy Studies, Dehradun, India.

<sup>5</sup>Department of Earth and Planetary Sciences, Harvard University, Cambridge, MA, USA.

<sup>6</sup>School of Engineering and Applied Sciences, Harvard University, Cambridge, MA, USA.

<sup>7</sup>NASA Goddard Space Flight Center, Greenbelt, MD, USA.

<sup>8</sup>Department of Ecology, Evolution, and Environmental Biology, Columbia University, New York, NY, USA.

\*Correspondence to: [rgautam@edf.org](mailto:rgautam@edf.org)

†These authors contributed equally to this work.

### Abstract

Extreme smog in India widely impacts air quality in late autumn and winter months. While the links between emissions and air quality are well-recognized, the association of smog and its intensification with climatic trends in the lower troposphere, where aerosol pollution and its radiative effects manifest, are not understood well. Here we use long-term satellite data to show a significant increase in aerosol exceedances over northern India, resulting in sustained atmospheric warming and surface cooling over the last two decades. We find several lines of evidence suggesting these aerosol radiative effects have induced a multidecadal (1980-2019) strengthening of lower tropospheric stability and an increase in relative humidity, leading to over fivefold increase in poor visibility days. Given this crucial aerosol-radiation-meteorological feedback driving the smog intensification, we anticipate results from this study will help inform mitigation strategies supporting stronger region-wide measures, which are critical for solving the smog challenge in India.

## MAIN TEXT

### INTRODUCTION

Air pollution in India severely impacts air quality, public health and economy in one of the world's most densely populated regions (1-3). Persistent agricultural fires during late autumn period (4-10) and widespread winter-time pollution (11-16) contribute to the extreme smog over south Asia, especially affecting entire northern India. The late autumn and winter months are the worst smog periods, resulting in the largest degradation of air quality in the Indo-Gangetic Plains (IGP), where nearly one-seventh of the world's population lives across northern India, Pakistan, Nepal and Bangladesh. In recent years, northern India has witnessed some of the most intense smog spells with extremely low visibility and hazardous air quality. The persistent smog invariably attracts heightened public and media attention (17) owing to the anomalous levels of fine particulate matter (PM<sub>2.5</sub>) recorded between November and January, every year. For instance, daily PM<sub>2.5</sub> concentrations during agricultural burning, frequently exceed 200 µg/m<sup>3</sup>, an order of magnitude larger than the World Health Organization's air quality guideline (7-9,17). In

48 addition to health and economic impacts of pollution (1-3), impacts of smog include  
49 prolonged delays/cancellations of trains and flights, and even vehicular accidents in  
50 northern India (11,13,18).

51 While the worsening air quality in India has deservedly received growing attention, the  
52 linkages between smog intensification and climatic trends in the lower troposphere where  
53 aerosol pollution occurs, are not understood well. On the other hand, it is well known that  
54 sunlight-absorbing aerosols lead to atmospheric warming and surface cooling via aerosol  
55 radiative effects (19), thereby increasing the stability of the lower troposphere by inducing  
56 a temperature inversion (20,21). A stable lower troposphere implies reduced dispersion of  
57 pollutants leading to further accumulation of aerosols in the shallow boundary layer. Here,  
58 from an observational perspective, we examine lower-tropospheric changes during the last  
59 40 years to investigate such aerosol-radiation-meteorological feedbacks for gaining new  
60 insights into the extreme smog problem in northern India and unraveling its long-term  
61 intensification.

## 62 **RESULTS**

### 63 **Trends in aerosol-induced atmospheric warming and surface cooling**

64 We start with characterizing aerosol trends in northern India, where much of the agricultural  
65 burning occurs in the northwestern state of Punjab, the so-called breadbasket of the country  
66 and among the largest producing rice and wheat crop states nationally. Figure 1 shows the  
67 long-term climatology of satellite-derived aerosol optical depth (AOD), an indicator of  
68 aerosol loading, over south Asia averaged during the last two decades from MODIS  
69 observations (see data description in Materials and Methods). The spatial distribution of  
70 AOD indicates pronounced enhancement in the IGP, along the southern edge of the  
71 Himalaya. November is the dominant crop burning month in recent years when peak fire  
72 activity and subsequent aerosol loading has increased (6,9) and is separately shown from  
73 December-January mean (winter haze period) (Fig. 1). We find accelerated upward trends  
74 in November AOD, which are higher by a factor of  $>3$  relative to the annual-mean trend  
75 over northern India (fig. S1), leading to a  $\sim 90\%$  increase in November from 2002 to 2019  
76 (Fig. 2A).  
77

78  
79 In order to characterize changes in extreme smog, we report AOD exceedances (see  
80 Materials and Methods) indicating an even larger increase of  $\sim 140\%$  in November over  
81 northern India (Fig. 2B). This upsurge appears consistent with increase in agricultural fire  
82 activity, attributed to a government-mandated delay in transplanting of rice seedlings  
83 (contributing to increased burning in a shorter timespan) and expanded crop productivity in  
84 Punjab (6-9). With respect to the winter months, northern India experiences the largest  
85 aerosol loading ( $AOD > 0.8$ ) over central-eastern IGP (Fig. 1C), where population density  
86 is the highest across states of eastern Uttar Pradesh, Bihar and West Bengal. The winter  
87 smog is known to be associated with a shallow boundary layer, frequent temperature  
88 inversion, light winds and high relative humidity (11-16). Similar to November, although  
89 smaller in magnitude, we find significant positive trends in winter AOD (Fig. 1D and Fig.  
90 2A), which are  $>1.5$  times higher than the annually-averaged trend (fig. S1). There is a  
91  $>40\%$  rise in winter aerosol exceedances during the last two decades (Fig. 2B), with the  
92 largest increase of  $\sim 60\%$  in central-eastern IGP (Fig. 1D). We also find upward trends in  
93 ground-based and other satellite datasets (fig. S2, S3, S4), during both crop burning and  
94 winter haze, supporting the observation of intensification of aerosol pollution as detected in  
95 multiple disparate measurements.  
96

97 How does the increased aerosol pollution impact the regional radiation budget? We analyze  
98 the direct radiative effect of aerosols, specifically to characterize the impact of increasing  
99 AOD on surface cooling and atmospheric warming trends using solar radiation fluxes from  
100 CERES satellite observations (see Materials and Methods). A consistent increase is found  
101 in top-of-atmosphere (TOA) flux (fig. S5) and a reduction in surface-reaching radiation  
102 (implying surface cooling), corresponding to cloud-free aerosol-laden observations during  
103 the last two decades (Fig. 2C). An example of the relationship between collocated AOD and  
104 radiation fluxes (fig. S6), indicates a positive aerosol-induced effect at the TOA  
105 (brightening) and negative effect at surface (cooling). The surface cooling associated with  
106 crop burning and winter haze is evident across the IGP, leading to over 15-25%  
107 instantaneous reduction in solar insolation (Fig. S6, S7).

108  
109 Our central finding in the radiative effects analysis is the net increase in aerosol-induced  
110 surface cooling, from 2002 to 2019, is twice as large compared to the increase in TOA flux.  
111 This disparity implies that considerably less radiation is being reflected at TOA as a result  
112 of significant solar absorption within the aerosol layer, in turn causing the large surface  
113 cooling anomaly. This is consistent with the low aerosol single scattering albedo in northern  
114 India (22,23), indicative of an absorbing aerosol layer. The resulting aerosol-induced  
115 absorption (Fig. 2D) and atmospheric heating rate (fig. S8) is largely confined to the lowest  
116 ~1.5 km of the troposphere, where most of the aerosol layer resides during late autumn-  
117 winter in northern India, as indicated by spaceborne lidar observations (fig. S9). Overall,  
118 concurrent with enhanced surface cooling, there is a 70-80% increase in aerosol-induced  
119 lower tropospheric warming over the last two decades (Fig. 2C, 2D), suggesting an  
120 increasing tendency toward a stable lower troposphere, which favors buildup of aerosol  
121 pollution in the shallow boundary layer where emissions from agricultural fires and other  
122 anthropogenic sources occur.

### 123 **Strengthening of lower tropospheric stability and intensification of smog**

124 With aerosol-induced radiative effects evident in lower tropospheric warming and surface  
125 cooling, we then investigate whether long-term changes in atmospheric stability and related  
126 meteorological parameters have occurred in turn amplifying the smog intensification. Fig.  
127 3 shows the climatology and trends of lower tropospheric stability (LTS) (24), a measure of  
128 the strength of temperature inversion that caps the planetary boundary layer (see Materials  
129 and Methods). The IGP emerges under a strong LTS influence during late autumn and  
130 winter, based on the past four decades of meteorological data (Fig. 3a and fig. S10). The  
131 enhanced LTS is particularly evident over northern India, as part of an overall stable lower-  
132 tropospheric feature. We find a significant and sustained upward trend leading to an 18-  
133 25% increase in LTS over northern India from 1980 to 2019 (Fig. 3B).

134  
135  
136 Coincidentally, the number of poor visibility days (defined here as visibility < 1000 m) has  
137 increased fivefold over northern India during November and >2 times during December-  
138 January over the last 40 years (fig. S11). This worsening trend is even severe for days with  
139 much lower visibility (< 500 m), indicating a factor of >9 increase during the crop burning  
140 period and a fivefold increase in winter. Over Delhi, where pollution levels are among the  
141 highest in the world, the smog has undergone significant intensification (at least a fivefold  
142 increase for visibility < 500 m), with poor visibility largely dominating the late autumn-  
143 winter periods since the 1990s (Fig. 3C, 3D). The degrading visibility is accompanied by a  
144 systematic 20% increase in near-surface relative humidity (RH), over the last four decades,  
145 with high RH (85%-95%) observed in recent years (Fig. 3E). The association between RH  
146 and poor visibility indicates a higher correlation ( $r$ : 0.77–0.85,  $p$ -value  $\ll$  0.01) for days

147 with visibility < 500 m (fig. S12), supporting the observation of enhanced visibility  
148 degradation under humid conditions.

149  
150 Overall, there appears to be an aerosol-radiation-meteorological feedback mechanism  
151 playing a potentially crucial role towards smog intensification whereby aerosol-induced  
152 atmospheric warming and surface cooling lead to the stability of the lower troposphere.  
153 Increased stability means capping of pollutants and further increase in aerosol  
154 concentrations in the shallow planetary boundary layer (PBL); at the same time entrainment  
155 of dry air from the free troposphere decreases, causing enhanced moisture availability in the  
156 PBL and higher RH (16,20). The increase in RH enhances aerosol scattering mediated by  
157 the hygroscopic growth of aerosols, and promotes formation of secondary aerosols, further  
158 exacerbating the severity of smog (12,21). We also find indication of the contraction of PBL  
159 in recent decades (see Materials and Methods and fig. S13), suggesting a moistened shallow  
160 boundary layer favorable for persistence of smoggy conditions.

161  
162 The increase in RH could also in part be linked to the increase in irrigated area in the IGP;  
163 irrigation in India has expanded 2-3 times since the 1970s and may contribute to the  
164 enhanced moisture in the PBL (25). Regardless of the cause, smog intensification appears  
165 to be amplified by aerosol-radiation-meteorological feedbacks, as observed in the increasing  
166 trends of aerosol-induced atmospheric warming and surface cooling, along with the long-  
167 term strengthening of lower tropospheric stability and concurrent trends in RH and visibility  
168 degradation during the last 40 years.

169  
170 It is noteworthy that extreme smog episodes in November, coinciding with agricultural  
171 burning, arrive in advance of the peak winter smog season in the IGP. As an illustration of  
172 the aerosol-radiation-meteorological coupling, Fig. 4A shows the evolution of a dense smog  
173 spell with thick haze around the beginning of November 2017, transforming into foggy  
174 conditions that altogether persisted for almost three weeks. The smog was so severe across  
175 northern India that the peak PM<sub>2.5</sub> concentrations reached ~1,000 µg/m<sup>3</sup> in Delhi, prompting  
176 the closure of 4,000 schools (4) and a major international airliner to suspend its flight  
177 operations into the city (26). In another recent smog-filled episode, an international cricket  
178 match (most popular sport in south Asia) was halted probably for the first time in the sports'  
179 history due to smog, with players visibly sick and wearing pollution masks on the field (27).  
180 This intense degradation in air quality and visibility could have been amplified by a  
181 pronounced temperature inversion and high relative humidity in the lower troposphere (Fig.  
182 4B). We also analyzed 40 years of radiosonde observations of daily temperature profiles  
183 and found a twofold increase in the frequency of lower tropospheric temperature inversion  
184 (Fig. 4), consistent with upward trends in LTS, visibility degradation and RH (Fig. 3).

## 185 186 **DISCUSSION**

187 Such extreme events serve as examples of the heightened attention the smog problem has  
188 increasingly received. On the other hand, there seems to be a lack of clarity regarding  
189 sources and transport mechanisms across states and countries in south Asia (28,29), which  
190 could be limiting effective measures to curb the pollution. In addition, connections of large-  
191 scale climatic patterns and interannual variability of aerosol pollution (15) may further add  
192 to the complexity of characterizing smog and its long-term intensification. Furthermore, the  
193 possible role of climate variability in contributing to poor ventilation conditions, suggested  
194 as conducive for extreme haze formation in China (30), may be worth investigating for  
195 studying severe pollution episodes in India. Such an analysis would benefit from large-scale  
196 climate model simulations involving land-atmosphere-cryosphere interactions (30), beyond

197 the observational findings this study has provided based on the synthesis of long-term  
198 satellite, surface and reanalysis datasets covering the past four decades.

199  
200 The government of India, in October 2020, promulgated a major commission on air quality  
201 management in the national capital region (NCR) around Delhi and adjoining areas (31).  
202 This initiative distinctly recognizes the air pollution challenge in NCR; where adjoining  
203 areas are defined as “where any source of pollution is located causing adverse impact of air  
204 quality in the NCR” (31). As our results indicate, the increasing aerosol pollution and  
205 radiative impacts, clearly extend beyond NCR (<60 million population) and encompass the  
206 whole of northern India, affecting both the urban and the vast rural populations (over 600  
207 million population of Indian states in the IGP).

208  
209 While reductions in emissions are known to have led to significant air quality  
210 improvements across broad regions of Europe, North America, and East Asia (32,33), the  
211 long-term rise in extreme smog over northern India is particularly concerning and in turn  
212 provides an opportunity to strengthen mitigation action. The northern Indian region, as  
213 part of the broader IGP, lies in a valley-type terrain immediately south of the towering  
214 Himalaya and so is naturally vulnerable to pollution build-up. Given the likely role of  
215 aerosol-radiation-meteorological feedbacks in worsening the widespread smog, expanding  
216 upon current air quality improvement efforts by accounting for pollution sources and  
217 transport processes across entire northern India, will support the development of a region-  
218 wide mitigation strategy.

## 220 MATERIALS AND METHODS

### 221 Datasets

222 We used two decades of multi-satellite observations to characterize trends in aerosol optical  
223 depth (AOD) and associated aerosol-induced radiative forcing during crop burning  
224 (November) and winter haze periods (December-January) over northern India.

225 Moderate resolution Imaging Spectroradiometer (MODIS) AOD data-

226 We used the 10 km x 10 km spatial resolution MODIS Level-2 Collection 6.1 (C061)  
227 quality-assured daily aerosol retrievals (MOD04 and MYD04) at 550 nm from both Terra  
228 (20 years; 2000-2019) and Aqua (18 years; 2002-2019) over the Indo-Gangetic Plains (IGP).  
229 The Terra local overpass time is ~10:30 am and Aqua is ~1:30 pm. We used AOD retrievals  
230 from the Deep Blue (DB) algorithm for characterizing the climatology and trends in AOD  
231 during crop burning (November) and winter haze (December-January) periods. The  
232 uncertainty for DB AOD retrievals is reported as  $\pm(0.03 + 0.2\tau)$  (34), where  $\tau$  represents  
233 AOD. Details of the DB AOD data product are available at-

234 [https://modis-](https://modis-atmos.gsfc.nasa.gov/sites/default/files/ModAtmo/modis_deep_blue_c61_changes.pdf)  
235 [atmos.gsfc.nasa.gov/sites/default/files/ModAtmo/modis\\_deep\\_blue\\_c61\\_changes.pdf](https://modis-atmos.gsfc.nasa.gov/sites/default/files/ModAtmo/modis_deep_blue_c61_changes.pdf).

236 We computed exceedances in AOD which are defined here as the mean of daily pixel-level  
237 data found above +1 standard deviation of the spatial mean AOD computed individually for  
238 each time period (i.e. separately for crop burning and winter haze periods), and then repeated  
239 for each year. These AOD exceedances were analysed for their trends to characterize long-  
240 term changes in extreme aerosol pollution over the IGP using Aqua and Terra MODIS  
241 observations during the past two decades (as depicted in Fig. 2b and fig. S3). The MODIS  
242 aerosol data used in this study is available from: <https://ladsweb.modaps.eosdis.nasa.gov/>.

## 243 Clouds and the Earth's Radiant Energy System (CERES) data-

244 To characterize changes in aerosol-induced radiative effects, the most recent Edition 4  
 245 CERES Single Scanner Footprint (SSF) Level-2 data product, from Aqua satellite at 20 km  
 246 x 20 km horizontal resolution at nadir (18 years; 2002-2019), is used for evaluating the  
 247 impacts of aerosol loading on clear-sky top-of-atmosphere (TOA) and surface shortwave  
 248 radiative fluxes during crop burning and winter haze periods. The Aqua/CERES daytime  
 249 overpass is ~1:30 pm local-time. The CERES instrument measures radiance at a given Sun-  
 250 satellite geometry, which is then converted to radiative flux using angular distribution  
 251 models. More details about the CERES instrument and its calibration are discussed  
 252 elsewhere (35). The averaged TOA instantaneous shortwave flux uncertainty is reported to  
 253 be 1.6 % ( $4.5 \text{ W m}^{-2}$ ) for cloud-free scenes over land surfaces (36). Instantaneous footprints  
 254 of TOA radiances are operationally used as a constraint to compute the surface radiative  
 255 fluxes following the NASA Langley Fu-Liou radiative transfer model. The CERES-derived  
 256 surface fluxes have been extensively validated over the past two decades against ground-  
 257 based shortwave flux measurements from high-quality surface networks. The uncertainty in  
 258 the cloud-free surface flux data product based on global assessment (37) is associated with  
 259 a systematic error of  $-0.6 \text{ W m}^{-2}$  ( $-0.1 \%$ ) and a random error of  $37.5 \text{ W m}^{-2}$  ( $6.1 \%$ ), with  
 260 the relative error as included in the parenthesis. For continental scenes, the cloud-free  
 261 surface flux uncertainty is reported with a systematic error of  $6.3 \text{ W m}^{-2}$  ( $0.9 \%$ ) and random  
 262 error of  $49.9 \text{ W m}^{-2}$  ( $7.1 \%$ ) (37). More information about the CERES SSF data product is  
 263 available at:

264 [https://asdc.larc.nasa.gov/documents/ceres/quality\\_summaries/CER\\_SSF\\_Terra-](https://asdc.larc.nasa.gov/documents/ceres/quality_summaries/CER_SSF_Terra-Aqua_Edition4A.pdf)  
 265 [Aqua\\_Edition4A.pdf](https://asdc.larc.nasa.gov/documents/ceres/quality_summaries/CER_SSF_Terra-Aqua_Edition4A.pdf). The CERES SSF data used in this study is available from:  
 266 <https://ceres.larc.nasa.gov/data/#ssf-level-2>.

## 267 European Centre for Medium-Range Weather Forecasts (ECMWF) ERA5 reanalysis data-

268 To examine long-term trends in the lower tropospheric stability over the IGP, we used  
 269 reanalysis meteorological fields from the ECMWF ERA5 dataset. The reanalysis is  
 270 produced using the Integrated Forecast System (IFS) cycle 41r2 with 4D-Var data  
 271 assimilation, as released in 2016. ERA5 has a horizontal resolution of  $0.25^\circ \times 0.25^\circ$ ,  
 272 available at 137 hybrid sigma pressure levels in the vertical domain (from 1000 to 0.01 hPa).  
 273 Details about the atmospheric models, assimilation methodology, improvements and quality  
 274 of the data are extensively discussed elsewhere (38). In this study, we extracted the air  
 275 temperature data for three different pressure levels (700 hPa, 850 hPa and 1000 hPa) to  
 276 derive lower tropospheric stability at 700 hPa and 850 hPa. The ERA5 data is available  
 277 from: <https://www.ecmwf.int/en/forecasts/datasets/reanalysis-datasets/era5>.

## 278 Radiosonde data &amp; ground-based observations

279 Radiosonde observations are obtained from the NOAA land-based radiosonde station  
 280 network - Integrated Global Radiosonde Archive (IGRA) (39). For this study, we used the  
 281 enhanced version 2 of IGRA database (40) which contains data on temperature, geopotential  
 282 height, relative humidity and wind at various atmospheric pressure levels, as well as  
 283 additional derived moisture variables and calculated vertical gradients of several other  
 284 variables. A detailed description of the IGRA datasets as well as information on quality  
 285 assurance are discussed elsewhere (39). We used radiosonde data at 5 locations throughout  
 286 northern India (Patiala –  $30.33^\circ\text{N}/76.47^\circ\text{E}$ , Safdarjung –  $28.58^\circ\text{N}/77.2^\circ\text{E}$ , Gorakhpur –  
 287  $26.75^\circ\text{N}/83.37^\circ\text{E}$ , Lucknow –  $26.75^\circ\text{N}/80.88^\circ\text{E}$ , Patna –  $25.6^\circ\text{N}/85.17^\circ\text{E}$ ), representing  
 288 observations from the western end of the Gangetic Plains (Patiala) to the eastern portion  
 289 (Patna) to assess trends in the planetary boundary layer (PBL) height. We also obtained PBL  
 290 data from NASA's Modern-Era Retrospective analysis for Research and Applications,

version 2 (MERRA-2) to additionally analyze long-term changes in PBL over the IGP; MERRA-2 data are available from <https://gmao.gsfc.nasa.gov/reanalysis/MERRA-2/>.

Additionally, we used ground-based weather station data at five sites (as mentioned above) from northern India to characterize long-term trends in visibility and relative humidity (RH) for the period 1980-2019, based on surface meteorological observations from the global archive data obtained from NOAA's National Climatic Data Center's Climate Data Online program (<https://www.ncdc.noaa.gov/cdo-web/>).

Finally, we also used Multi-angle Imaging Spectro-Radiometer (MISR) Level-3 AOD data at  $0.5^\circ \times 0.5^\circ$  (<https://giovanni.gsfc.nasa.gov/giovanni/>) and AERONET level-2 AOD data from Kanpur (<https://aeronet.gsfc.nasa.gov/>).

### Aerosol radiative forcing

Data from the CERES instrument onboard Aqua satellite was used to characterize the radiative impact of aerosols on shortwave fluxes at the TOA and surface. The CERES observations were gridded onto a  $0.25^\circ \times 0.25^\circ$  uniform grid on a daily basis and collocated with MODIS quality-assured Deep Blue AOD in space and time (best quality AOD retrievals were used to ensure stringent cloud filtering). The CERES derived fluxes were normalized by the cosine of solar zenith angle. In this study, northern India is divided into seven equal-spaced,  $2^\circ \times 2^\circ$  grids, traversing from the western edge of the Gangetic Plains to the eastern flank (fig. S6).

The clear-sky shortwave aerosol radiative forcing ( $\Delta F$ ) at the TOA and surface (SFC) is defined as the net change in shortwave radiative flux caused by aerosols which is calculated as:

$$\Delta F_{TOA/SFC} = (F_a)_{TOA/SFC} - (F_{na})_{TOA/SFC} \quad (1)$$

where,  $F_a$  is the clear-sky shortwave flux at TOA and surface in the presence of aerosol-laden atmosphere (i.e. AOD > 0).  $F_{na}$  represents the radiative fluxes without the presence of aerosols and is derived from the  $y$ -intercept (at AOD = 0) of the linear regression between daily MODIS AOD and instantaneous CERES shortwave fluxes at the TOA and surface for each subregion and year, during the crop burning and winter haze (fig. S6). This approach has been used in previous studies for characterizing direct radiative effect of aerosols (41,42). The negative values of  $\Delta F$  at surface imply that aerosols induce a cooling effect; whereas positive values at TOA are indicative of a brightening effect at TOA.  $F_{na}$  is computed only for those grid-cells where the number of data points is more than 10 and solar zenith angle less than  $60^\circ$ . In addition, the magnitude of solar radiation absorbed by aerosols within the atmosphere ( $\Delta F_{atm} = \Delta F_{TOA} - \Delta F_{SFC}$ ) was computed, which defines the net atmospheric forcing (ATM) induced by aerosol absorption in the atmosphere. We also calculate the instantaneous atmospheric heating rate (K/day), due to absorption of solar radiation by aerosols, based on the first law of thermodynamics and hydrostatics equilibrium as follows:

$$\frac{\partial T}{\partial t} = \frac{g}{C_p} \times \frac{\Delta F_{atm}}{\Delta P} \quad (2)$$

where,  $\partial T/\partial t$  is the heating rate (K/day),  $g$  is the acceleration due to gravity,  $C_p$  is the specific heat capacity of air at constant pressure and  $\Delta P$  is the atmospheric pressure difference between the top and bottom of the atmospheric layer in which most of the aerosol loading resides. Here, we consider the lowest  $\sim 1.5$  km tropospheric layer as the prominent aerosol layer during the crop burning and winter haze periods, as indicated by the vertical distribution analysis of aerosol extinction data (fig. S9) from the NASA CALIPSO satellite's

Cloud-Aerosol Lidar with Orthogonal Polarization (CALIOP data obtained from <https://subset.larc.nasa.gov/calipso/>).

In addition to the CERES and MODIS data derived instantaneous aerosol radiative forcing and heating rates, we also compute the diurnal mean (24-hour mean) aerosol radiative forcing and heating rates using a 1-dimensional plane-parallel radiative transfer model (RTM) (43). We used the observed relationship between TOA shortwave flux and AOD from CERES and MODIS data, respectively, specifically the slope and offset of the linear regression to constrain the RTM-calculated fluxes including the aerosol optical properties including single scattering albedo and asymmetry parameter. The aerosol optical properties were also constrained by data from ground-based column aerosol retrievals from NASA's AERONET sites in the IGP. Additionally, the aerosol vertical distribution input to the RTM was based on climatology of CALIPSO measurements (indicating most of the aerosol extinction with the surface to ~1.5 km tropospheric layer). The RTM calculations were performed at every one degree increments of solar zenith angle to compute the radiative forcing and heating rate. The diurnal mean aerosol-induced heating rate averaged over the IGP for the 18-year period for the period 2002-2019 is 1.4 K/day – 1.6 K/day for the crop burning and winter haze periods. We find that the heating rate in the crop burning period has increased by ~85% (to 2.1 K/day) and in the winter haze period by ~37% (to 1.7 K/day) during the 18-year period. This enhancement in aerosol-induced heating in the lower troposphere, including the varying trend magnitudes by the different periods, are consistent with the observations of increase in AOD (mean and exceedances) as well as the aerosol-induced aerosol absorption, i.e. larger aerosol-induced absorption and heating trends in November relative to December-January (Fig. 2).

### Boundary layer height and frequency of temperature inversion

The PBL height in the IGP, during the crop burning and winter haze periods, was derived using the bulk Richardson number ( $R_i$ ) method (44). The estimation of PBL height involved data obtained from NOAA IGRA as aforementioned in the Datasets section. Details of the bulk  $R_i$  method and the criteria to derive PBL heights along with an uncertainty analysis and a comparison with other methods are discussed elsewhere (45). The following equation provides the main physical relationships involved in the computation of PBL heights:

$$Ri(z) = \frac{(g/\theta_{vs})(\theta_{vz}-\theta_{vs})(z-z_s)}{((u_z-u_s)^2+(v_z-v_s)^2+(bu_*^2)} \quad (3)$$

where,  $z$  is altitude of the atmospheric and  $z_s$  denotes the surface altitude,  $g$  is acceleration due to gravity,  $\theta_v$  is virtual potential temperature,  $u$  and  $v$  are the horizontal components of the wind speed,  $b$  is a constant and  $u_*$  is the surface friction velocity. Since  $u_*$  is not known from radiosonde data, we set  $b = 0$  and thus ignore surface friction effects, which are very small in comparison to the bulk shear terms in the denominator (46). The lowest level  $z$  at which interpolated  $R_i$  crosses the critical threshold value of 0.25, determines the PBL height (45). For the estimation of PBL height, we used a threshold of at least five vertical levels available in daily radiosonde profiles greater than 500 hPa (i.e. between ground and 500 hPa). Since the vertical distribution of wind measurements prior to year 2000 over several radiosonde sites over northern India have uneven or relatively sparse coverage, we considered the PBL height analysis from 2000 onwards. During the last two decades, the PBL height (in meters) was found to be associated with a decreasing trend of  $-3.3 \pm 1.7 \text{ m yr}^{-1}$  (at 0Z or 5:30 am local-time) for the period 2000-2019, averaged for November-December-January over the five meteorological stations based on radiosonde observations. We also analysed MERRA-2 data over the entire northern India from and found an area-averaged trend of  $-10.7 \pm 2.9 \text{ m yr}^{-1}$  for the period 1995-2019 (fig. S13).



383 Regarding the computation of temperature inversion, the long-term data record and linear  
 384 trends in the frequency of temperature inversion (i.e. number of inversion instances) in the  
 385 lower troposphere was derived from daily radiosonde observations of temperature profiles  
 386 over Delhi for the 40-year period 1980-2019, during the crop burning (November) and  
 387 winter haze (December-January) periods. The trends in the frequency of temperature  
 388 inversion events (Fig. 4c,d) indicate a twofold increase in inversion frequency during the  
 389 last four decades for both November and December-January periods. The temperature  
 390 inversion was calculated from temperature profiles within the lower troposphere only,  
 391 defined here between ground-level and 700 hPa (or upto ~3 km above ground). The  
 392 radiosonde observations correspond to OZ (5:30 am local-time). The frequency of  
 393 inversion (y-axis) represents the monthly count of the total number of detected inversion  
 394 layers, in daily temperature profiles, which include both near-surface inversion and  
 395 elevated inversion layers (i.e. all inversion layers detected within the lower troposphere).  
 396 Note, multiple inversion layers can be present in a single radiosonde profile. The  
 397 methodology for characterizing inversion layer is similar to Kahl *et al.* (46) and Gilson *et*  
 398 *al.* (47). If one or more inversion layers are detected within <100 meters of the daily  
 399 vertical temperature profile, those layers are considered as a single inversion layer.

## 402 References

- 403 1. A. Pandey *et al.*, Health and economic impact of air pollution in the states of India: the  
 404 Global Burden of Disease Study 2019. *Lancet Planet. Heal.* **5**, e25–e38 (2021).
- 405 2. S. Chakrabarti, M. T. Khan, A. Kishore, D. Roy, S. P. Scott, Risk of acute respiratory  
 406 infection from crop burning in India: Estimating disease burden and economic welfare  
 407 from satellite and national health survey data for 250 000 persons. *Int. J. Epidemiol.* **48**,  
 408 1113–1124 (2019).
- 409 3. S. Chowdhury, S. Dey, K.R. Smith, Ambient PM 2.5 exposure and expected premature  
 410 mortality to 2100 in India under climate change scenarios. *Nat. Comm.*, **9**, 1-10 (2018).
- 411 4. P. Shyamsundar *et al.*, Fields on fire: Alternatives to crop residue burning in India.  
 412 *Science* **365**, 536-538 (2019). doi:10.1126/science.aaw4085.
- 413 5. S. Bikkina, A. Andersson, E.N. Kirillova, H. Holmstrand, S. Tiwari, A.K. Srivastava,  
 414 D.S. Bisht, Ö. Gustafsson, Air quality in megacity Delhi affected by countryside biomass  
 415 burning. *Nat. Sustain.* **2**, 200–205 (2019).
- 416 6. T. Liu, L.J. Mickley, R. Gautam, M.K. Singh, R.S. DeFries, M.E. Marlier, Detection of  
 417 delay in post-monsoon agricultural burning across Punjab, India: potential drivers and  
 418 consequences for air quality. *Environ. Res. Lett.* **16**, 014014 (2021). doi:10.1088/1748-  
 419 9326/abcc28.
- 420 7. D.H. Cusworth, L.J. Mickley, M.P. Sulprizio, T. Liu, M.E. Marlier, R.S. DeFries, S.  
 421 Guttikunda, P. Gupta, Quantifying the influence of agricultural fires in northwest India  
 422 on urban air pollution in Delhi, India. *Environ. Res. Lett.* **13**, 044018 (2018).
- 423 8. Balwinder-Singh, A.J. McDonald, A.K. Srivastava, B. Gerard, Tradeoffs between  
 424 groundwater conservation and air pollution from agricultural fires in northwest  
 425 India. *Nat. Sustain.* **2**, 580–583 (2019). <https://doi.org/10.1038/s41893-019-0304-4>.
- 426 9. H. Jethva, O. Torres, R.D. Field, A. Lyapustin, R. Gautam, V. Kayetha, Connecting  
 427 Crop Productivity, Residue Fires, and Air Quality over Northern India. *Sci.*  
 428 *Rep.* **9**, 16594 (2019). <https://doi.org/10.1038/s41598-019-52799-x>.

- 429 10. R. Kumar, S.D. Ghude, M. Biswas, C. Jena, S. Alessandrini, S. Debnath, S. Kulkarni, S.  
430 Sperati, V.K. Soni, R.S. Nanjundiah, M. Rajeevan, Enhancing accuracy of air quality  
431 and temperature forecasts during paddy crop residue burning season in Delhi via  
432 chemical data assimilation. *J. Geophys. Res. Atmos.* **125**, e2020JD033019 (2020).  
433 [https://doi.org/ 10.1029/2020JD033019](https://doi.org/10.1029/2020JD033019).
- 434 11. R. Gautam, N.C. Hsu, M. Kafatos, S.C. Tsay, Influences of winter haze on fog/low cloud  
435 over the Indo-Gangetic plains. *J. Geophys. Res.* **112**, D05207  
436 (2007). <https://doi.org/10.1029/2005JD007036>.
- 437 12. X. Pan *et al.*, A multi-model evaluation of aerosols over South Asia: common problems  
438 and possible causes. *Atmos. Chem. Phys.* **15**, 5903–5928 (2015).  
439 <https://doi.org/10.5194/acp-15-5903-2015>, 2015.
- 440 13. S.D. Ghude *et al.*, Winter fog experiment over the Indo-Gangetic plains of India. *Curr.*  
441 *Sci.* **112**, 767– 784 (2016). <https://doi.org/10.18520/cs/v112/i04/767-784>.
- 442 14. C. Venkataraman, A. Sharma, K. Tibrewal, S. Maity, K. Muduchuru, “Carbonaceous  
443 Aerosol Emissions Sources Dominate India’s Wintertime Air Quality”. EM (2019).  
444 <https://pubs.awma.org/flip/EM-Dec-2019/venkataraman.pdf>.
- 445 15. M. Gao, P. Sherman, S. Song, Y. Yu, Z. Wu, M. B. McElroy, Seasonal prediction of  
446 Indian wintertime aerosol pollution using the ocean memory effect. *Sci. Adv.* **5**,  
447 eaav4157 (2019).
- 448 16. V.S. Nair, F. Giorgi, U.K. Hasyagar, Amplification of South Asian haze by water  
449 vapour–aerosol interactions. *Atmos. Chem. Phys.* **20**, 14457-14471 (2020).
- 450 17. CNN, “New Delhi is choking on smog and there's no end in sight” (4 November 2019  
451 <https://www.cnn.com/2019/11/04/india/delhi-india-smog-pollution-intl-hnk/index.html>).
- 452 18. National Geographic, “Pollution Is So Bad in India, It's Causing Car Crashes” (13  
453 November 2017, YouTube video; [https://www.youtube.com/watch?v=r\\_vQDa42tuM](https://www.youtube.com/watch?v=r_vQDa42tuM)).
- 454 19. V. Ramanathan, P. J. Crutzen, J. T. Kiehl, D. Rosenfeld, Aerosols, climate, and the  
455 hydrological cycle. *Science* **294**, 2119-2124 (2001).
- 456 20. Z. Li, J. Guo, A. Ding, H. Liao, J. Liu, Y. Sun, T. Wang, H. Xue, H. Zhang, B. Zhu,  
457 Aerosol and boundary-layer interactions and impact on air quality. *National Science*  
458 *Review* **4**, 810-833 (2017).
- 459 21. Z. An, R. J. Huang, R. Zhang, X. Tie, G. Li, J. Cao, W. Zhou, Z. Shi, Y. Han, Z. Gu, Y.  
460 Ji, Severe haze in northern China: A synergy of anthropogenic emissions and  
461 atmospheric processes. *Proc. Nat. Acad. Sciences* **116**, 8657-8666 (2019).
- 462 22. D.G. Kaskaoutis, S. Kumar, D. Sharma, R.P. Singh, S.K. Kharol, M. Sharma, A.K.  
463 Singh, S. Singh, A. Singh, D. Singh, Effects of crop residue burning on aerosol  
464 properties, plume characteristics, and long-range transport over northern India. *J.*  
465 *Geophys. Res. Atmos.* **119**, 5424–5444 (2014). <https://doi.org/10.1002/2013JD021357>.
- 466 23. Z. Li, L. Li, F. Zhang, D. Li, Y. Xie, H. Xu, Comparison of aerosol properties over  
467 Beijing and Kanpur: Optical, physical properties and aerosol component composition  
468 retrieved from 12 years ground-based Sun-sky radiometer remote sensing data. *J.*  
469 *Geophys. Res. Atmos.* **120**, 1520– 1535 (2015).
- 470 24. R. Wood, C.S. Bretherton, On the relationship between stratiform low cloud cover and  
471 lower-tropospheric stability. *J. Clim.* **19**, 6425-6432 (2006).

- 472 25. A.K. Ambika, V. Mishra, Substantial decline in atmospheric aridity due to irrigation in  
473 India. *Environ. Res. Lett.* **15** 124060 (2020).
- 474 26. CNN, “United suspends flights to smog-filled Delhi” (10 November 2017  
475 <https://money.cnn.com/2017/11/10/news/delhi-pollution-united-flights/index.html>).
- 476 27. The Guardian, “Pollution stops play at Delhi Test match as bowlers struggle to breathe.  
477 (3 December 2017; [https://www.theguardian.com/world/2017/dec/03/pollution-stops-  
478 play-at-delhi-test-match-as-bowlers-struggle-to-breathe](https://www.theguardian.com/world/2017/dec/03/pollution-stops-play-at-delhi-test-match-as-bowlers-struggle-to-breathe)).
- 479 28. The Hindu, “States should stop blaming each other on stubble burning, need to take it  
480 seriously: Arvind Kejriwal” (13 October 2020;  
481 [https://www.thehindu.com/news/cities/Delhi/states-should-stop-blaming-each-other-on-  
482 stubble-burning-need-to-take-it-seriously-arvind-kejriwal/article32843377.ece](https://www.thehindu.com/news/cities/Delhi/states-should-stop-blaming-each-other-on-stubble-burning-need-to-take-it-seriously-arvind-kejriwal/article32843377.ece)).
- 483 29. M.E. Miro, M.E. Marlier, R.S. Girven, “Transboundary Environmental Stressors on  
484 India-Pakistan Relations: An Analysis of Shared Air and Water Resources” (RAND  
485 Corporation, 2019; [https://www.rand.org/pubs/research\\_reports/RR2715.html](https://www.rand.org/pubs/research_reports/RR2715.html)).
- 486 30. Y. Zou, Y. Wang, Y. Zhang, J.-H. Koo, Arctic sea ice, Eurasia snow, and extreme winter  
487 haze in China. *Sci Adv.* **3**, e1602751 (2017).
- 488 31. The Gazette of India, Extraordinary, “The Commission for Air Quality Management In  
489 National Capital Region And Adjoining Areas Ordinance, 2020” (CG-DL-E-28102020-  
490 222804, Part II – Section 1, 2020;  
491 <http://www.egazette.nic.in/WriteReadData/2020/222804.pdf>).
- 492 32. R. Vautard, P. Yiou, G.J. van Oldenborgh, Decline of fog, mist and haze in Europe over  
493 the past 30 years. *Nat. Geosci.* **2**, 115–119 (2007). <https://doi.org/10.1038/ngeo414>.
- 494 33. M.S. Hammer et al., Global Estimates and Long-Term Trends of Fine Particulate Matter  
495 Concentrations (1998-2018). *Environ. Sci. Technol.* **54**, 7879–7890 (2020).  
496 doi:10.1021/acs.est.0c01764.
- 497 34. A.M. Sayer, N.C. Hsu, C. Bettenhausen, M.K. Jeong, G. Meister, Effect of MODIS terra  
498 radiometric calibration improvements on Collection 6 Deep blue aerosol products:  
499 Validation and terra/aqua consistency. *J. Geophys. Res.* **120**, 12,157– 12,174 (2015).  
500 doi:10.1002/2015JD023878.
- 501 35. N.G. Loeb, N. Manalo-Smith, W. Su, M. Shankar, S. Thomas, CERES top-of-  
502 atmosphere earth radiation budget climate data record: Accounting for in-orbit changes  
503 in instrument calibration. *Remote Sens.* **8**, 182 (2016). <https://doi.org/10.3390/rs8030182>.
- 504 36. W. Su, J. Corbett, Z. Eitzen, L. Liang, Next-generation angular distribution models for  
505 top-of-atmosphere radiative flux calculation from CERES instruments: Validation.  
506 *Atmos. Meas. Tech.* **8**, 3297–3313 (2015). <https://doi.org/10.5194/amt-8-3297-2015>.
- 507 37. D.P. Kratz, S.K. Gupta, A.C. Wilber, V.E. Sothcott, Validation of the CERES Edition-  
508 4A Surface-Only Flux Algorithms. *J. Appl. Meteor. Clim.* **59**, 281-295 (2020).
- 509 38. H. Hersbach et al., The ERA5 global reanalysis. *Q. J. R. Meteorol Soc.* **146**, 1999-2049  
510 (2020).
- 511 39. I. Durre, R.S. Vose, D.B. Wuertz, Overview of the integrated global radiosonde archive.  
512 *J. Clim.* **19**, 53-68 (2006).
- 513 40. I. Durre, X. Yin, Enhanced radiosonde data for studies of vertical structure. *Bull. Am.*  
514 *Meteor. Soc.* **89**, 1257-1262 (2008).

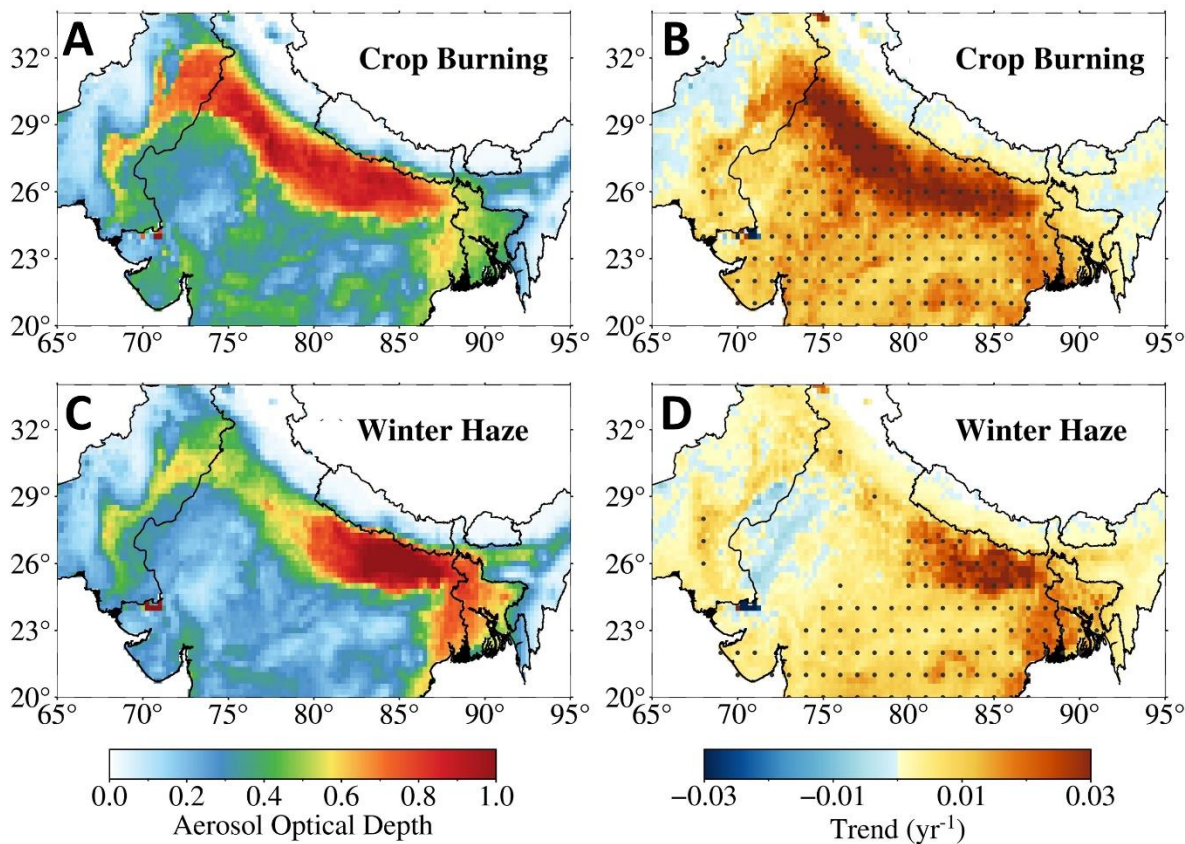
- 515 41. N.C. Hsu, J.R. Herman, C. Weaver, Determination of radiative forcing of Saharan dust  
516 using combined TOMS and ERBE data. *J. Geophys. Res. Atmos.* **105**, 20649-20661  
517 (2000).
- 518 42. R. Gautam, N.C. Hsu, T.F. Eck, B.N. Holben, S. Janjai, T. Jantarach, S.C. Tsay, W.K.  
519 Lau, Characterization of aerosols over the Indochina peninsula from satellite-surface  
520 observations during biomass burning pre-monsoon season. *Atmos. Environ.* **78**, 51-59  
521 (2013).
- 522 43. P. Ricchiazzi, S. Yang, C. Gautier, D. Sowle, SBDART: A research and teaching software  
523 tool for plane-parallel radiative transfer in the Earth's atmosphere. *Bulletin Amer.*  
524 *Meteorol. Soc.* **79**, 2101–2114 (1998).
- 525 44. P. Seibert, F. Beyrich, S.E. Gryning, S. Joffre, A. Rasmussen, P. Tercier, Review and  
526 intercomparison of operational methods for the determination of the mixing height.  
527 *Atmos. Environ.*, **34**, 1001-1027 (2000).
- 528 45. D.J. Seidel, Y. Zhang, A. Beljaars, J.-C. Golaz, A.R. Jacobson, B. Medeiros,  
529 Climatology of the planetary boundary layer over the continental United States and  
530 Europe, *J. Geophys. Res.* **117**, D17106 (2012). doi:10.1029/2012JD018143.
- 531 46. J.D. Kahl, M.C. Serreze, R.C. Schnell, Tropospheric low-level temperature inversions in  
532 the Canadian Arctic. *Atmosphere-Ocean* **30**, 511-529 (1992).
- 533 47. G.F. Gilson, H. Jiskoot, J.J. Cassano, T.R. Nielsen, Radiosonde-Derived Temperature  
534 Inversions and Their Association With Fog Over 37 Melt Seasons in East Greenland. *J.*  
535 *Geophys. Res. Atmos.*, **123**, 9571-9588 (2018).

## 536 537 **Acknowledgments**

538 **Funding:** This work was partly supported by Environmental Defense Fund. **Author**  
539 **contributions:** R.G. designed the study. P.N.P. and R.G. carried out the data analysis and  
540 interpretation with contributions from M.K.S. All authors discussed the results. R.G. wrote  
541 the manuscript. P.N.P., M.K.S., T.L., L.J.M., H.J. and R.D.S. reviewed, commented  
542 and/or edited the manuscript. **Competing interests:** Authors declare that they have no  
543 competing interests. **Data and materials availability:** All data underlying our study are  
544 available in the public domain. The MODIS data used in this study are available via  
545 [http://dx.doi.org/10.5067/MODIS/MYD04\\_L2.006](http://dx.doi.org/10.5067/MODIS/MYD04_L2.006) and CERES data are available via  
546 [https://doi.org/10.5067/Aqua/CERES/SSF-FM3\\_L2.004A](https://doi.org/10.5067/Aqua/CERES/SSF-FM3_L2.004A). We have provided links to the  
547 various data access portals in the Materials and Methods section for each of the satellite  
548 dataset, ground-based observations and modeling-based reanalysis datasets used in this  
549 study.  
550  
551  
552  
553  
554  
555  
556  
557  
558  
559

560  
561  
562  
563

## Figures

564  
565  
566  
567  
568  
569  
570  
571  
572  
573  
574  
575  
576  
577  
578  
579

**Fig. 1. Aerosol distribution and trends over south Asia during the last two decades using satellite data.** Aerosol optical depth (AOD) for crop burning (November) and winter haze (December-January) periods in (A) and (C), averaged from 2002-2019, using Aqua/MODIS observations. The AOD (unitless) is largest along the Indo-Gangetic Plains indicated by the warm shading. The corresponding linear trends in AOD (yr<sup>-1</sup>) are shown in (B) and (D), with dots indicating statistical significance of trends at 95% confidence level.

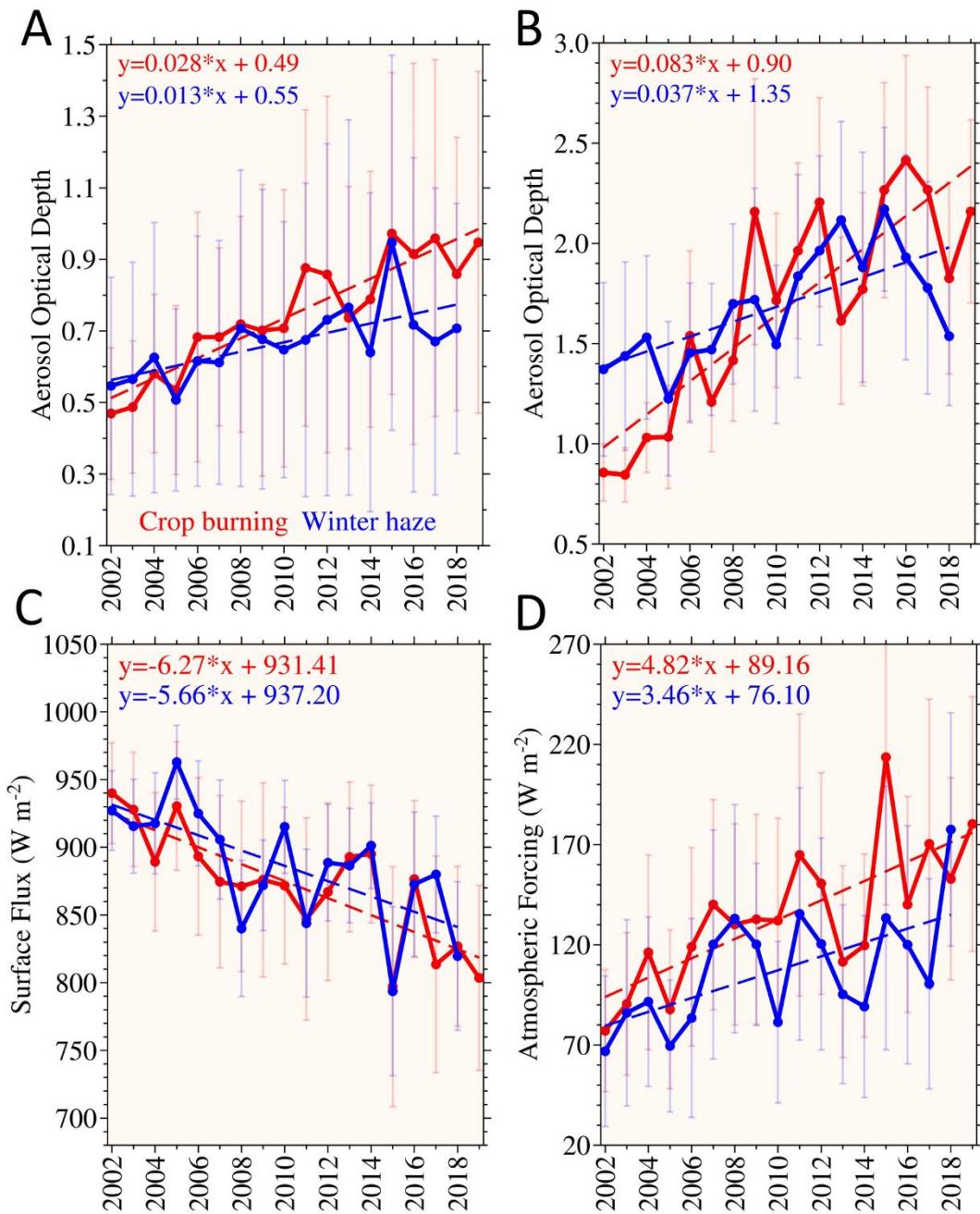


**Fig. 2. Trends in aerosol extremes, aerosol-induced surface cooling and atmospheric warming.** Time series and linear trends for (A) mean and (B) exceedance AOD, averaged over the Indo-Gangetic Plains for crop burning (red) and winter haze (blue) periods from 2002 to 2019. The corresponding trends in cloud-free collocated instantaneous shortwave fluxes, derived from Aqua/CERES observations, are shown in (C) surface cooling ( $\text{W/m}^2$ ) and (D) atmospheric forcing ( $\text{W/m}^2$ ) averaged over northern India. Error bars indicate  $\pm 1$  standard deviation.

580  
581  
582  
583  
584  
585  
586  
587  
588



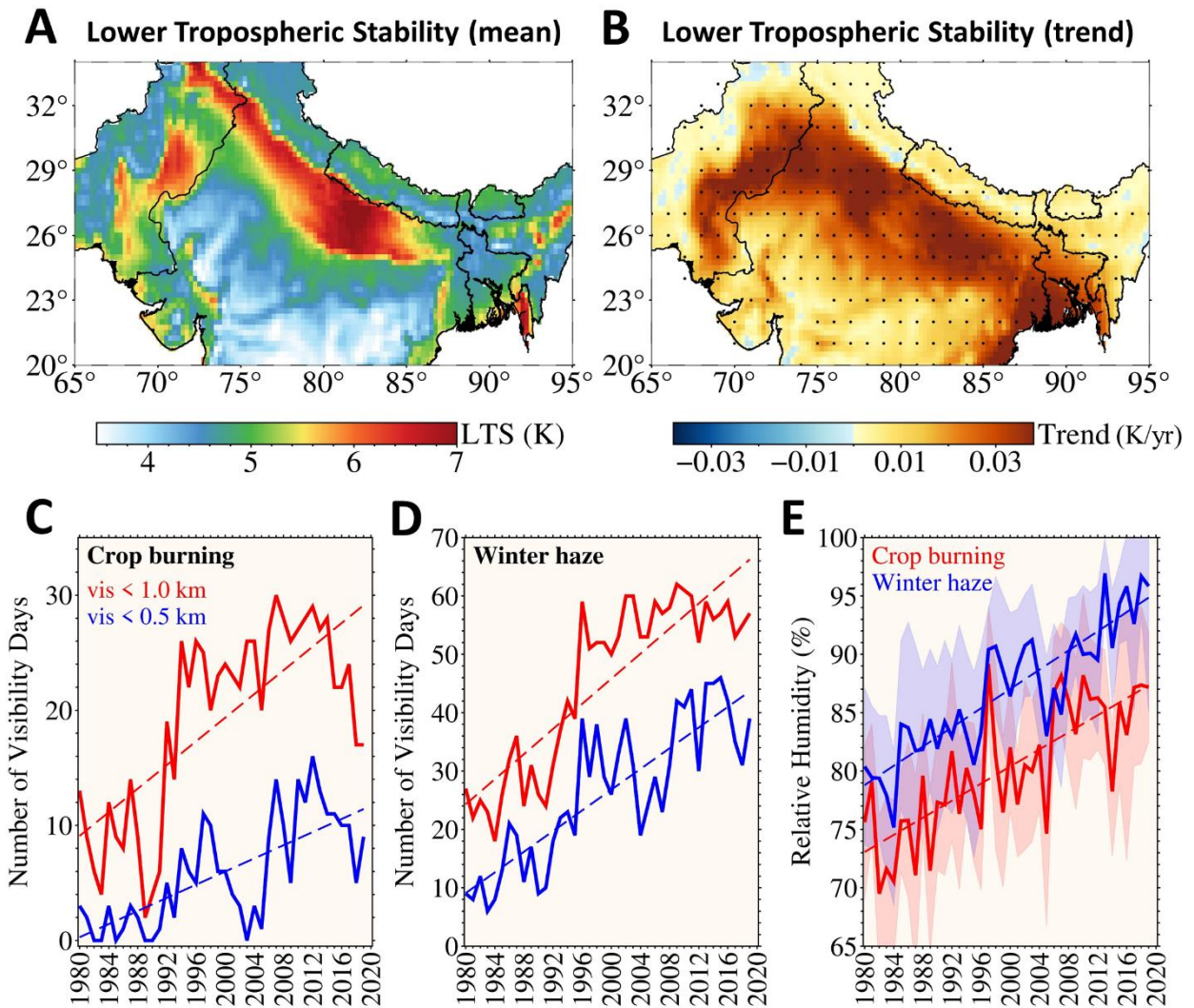


**Fig. 3. Lower tropospheric stability (LTS) and long-term trends in smog.** The LTS is shown as (A) the multidecadal average and (B) spatial trend, from November–January for the period 1980–2019, with significantly increasing LTS along the IGP. Dots in (b) indicate statistical significance of trends at 95% confidence level. Number of visibility days during (C) crop burning in November (out of 30 days) and (D) winter haze in December–January (out of 62 days) over Delhi. Visibility <1km is shown in red and <0.5km in blue. The monthly mean relative humidity (e) is shown for crop burning (red) and winter haze (blue) periods. Shading represents  $\pm 1$  standard deviation.

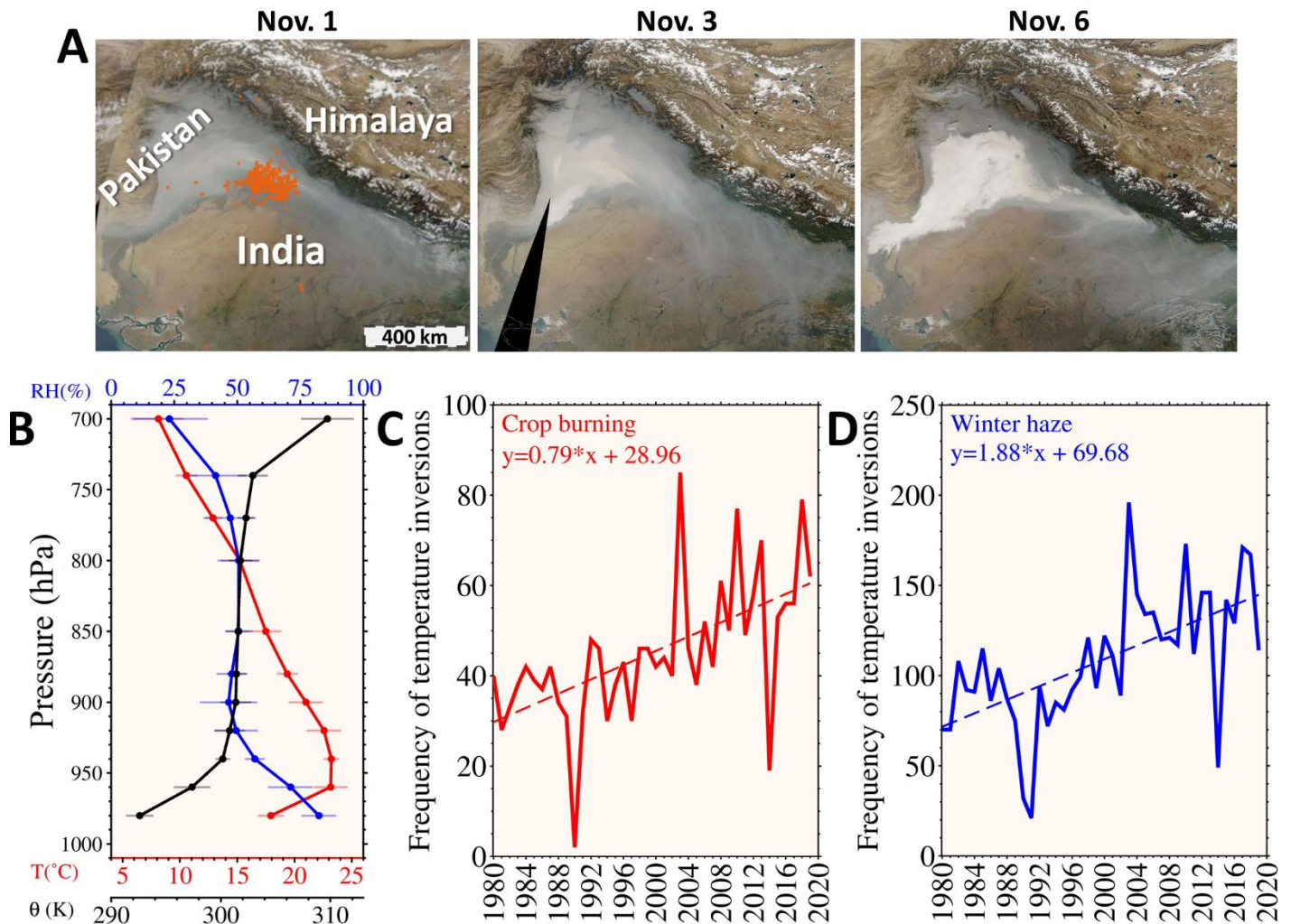


**Fig. 4. Evolution of smog blanketing southern Asia.** (A) An illustrative depiction of the evolution of smog in the Indo-Gangetic Plains, south of the Himalaya, encompassing Pakistan, northern India and Nepal. Satellite imagery (Terra/MODIS) is from 1, 3, 6 November 2017 acquired at ~10:30am local-time. Orange dots on 1 November show fire detections from Aqua/MODIS satellite observations (1:30pm local-time). (B) Vertical distribution of air temperature (red), potential temperature ( $\theta$  in black) and relative humidity (upper axis in blue), averaged from 31 October to 6 November 2017 (5:30am local-time), indicating pronounced temperature inversion and high relative humidity in the lowest tropospheric layers associated with smog occurrence. (C) and (D) Time series and linear trends in the frequency of temperature inversion (i.e. monthly count of the total number of detected inversion layers, in daily radiosonde observations) in the lower troposphere over Delhi from 1980 to 2019, for November (c) and December-January (d).